QNH: Mesoscale Bounded Derivative Initialization and Winter Storm Test over Complex Terrain

J. L. LEE

Forecast Systems Laboratory, NOAA/ERL/Boulder, Colorado and CIRA, Colorado State University, Foothills Campus, Fort Collins, Colorado

A. E. MacDONALD

CIRA, Colorado State University, Foothills Campus, Fort Collins, Colorado

ABSTRACT

Mesoscale bounded derivative initialization (BDI) is utilized to derive dynamical constraints, from which elliptic equations are formulated to derive smooth initial fields over complex terrain for mesoscale models. The initialization is implemented specifically for the quasi-nonhydrostatic (QNH) model. This study presents the first real data application of the mesoscale BDI and the QNH model to simulate a mesoscale storm that produced heavy precipitation along the Colorado Front Range. In this study, the focus is on (i) smooth numerical solution over complex terrain, (ii) baroclinic instability associated with condensational heating and high mountains, and (iii) the simulation of orographic precipitation. Numerical results show that initial fields derived from BDI were smooth and evolved smoothly in the QNH model for 48 h. It is noteworthy that the smooth solution existed up to the lateral boundaries. During the 48-h simulation, the midtropospheric storm moved freely in and out of the limited-area domain as if there were no lateral boundaries. The mesoscale storm for northeast Colorado was initiated by the persistent upslope easterlies and strong upward motions that triggered heavy precipitation. The simulated precipitation amounts and pattern were in good agreement with those observed. In general, both the large-scale dynamic system and the mesoscale precipitation event evolved smoothly and accurately, which indicates the value of BDI and QNH for mesoscale weather prediction.

1. Introduction

A quasi-nonhydrostatic (QNH) mesoscale weather prediction model has been developed recently at the National Oceanic and Atmospheric Administration's (NOAA's) Forecast Systems Laboratory. An important and unique aspect of this model is the use of bounded derivative initialization (BDI), which is the main subject of this paper. The mathematical theory associated with the QNH model is presented in MacDonald et al. (2000a), and the model description and test program are presented in MacDonald et al. (2000b). In this study, we show the first real data application for the QNH model. For real data simulations, an initialization scheme is necessary to attain smooth initial wind and mass fields that are compatible with numerical models (Bengtsson 1975). In most meteorological operational centers, initialization has been blended into the data assimilation system using dynamic models, with most

of the models being hydrostatic (Daley 1991). However, in many applications, initialization is needed to derive smooth initial fields for a mesoscale model (such as a nonhydrostatic model) from another model with different physics or dynamics (such as a hydrostatic model).

The purpose of this study is to formulate mesoscale BDI over complex terrain to derive smooth initial fields from other model grid data for a storm simulation using the QNH model. Both BDI and QNH were developed based on the mathematical theory of well-posedness; that is, the existence of a smooth solution (Kreiss 1980; Browning and Kreiss 1986). Smooth solution is important in providing a proper mathematical bound on the inevitable exponential error growth (Kreiss and Lorenz 1989) due to the truncation, data, and physical parameterization errors. One of the objectives in this study is to test the mathematical smoothness theory with BDI and QNH in the presence of a mesoscale snow storm. In this study, we applied the mesoscale BDI and the QNH model to simulate a mesoscale snow storm over the Rocky Mountains that occurred during 8–9 March 1992. It will be referred to as the 9 March storm. Detailed descriptions of the QNH model are given in Mac-Donald et al. (2000a,b). In the following, we describe

Corresponding author address: J. L. Lee, NOAA/ERL/Forecast Systems Laboratory, R/E/FS, 325 Broadway, Boulder, CO 80523. E-mail: jlee@fsl.noaa.gov

the bounded derivative initialization and the 9 March mesoscale storm.

Bounded derivative initialization is based on the bounded derivative principle (Kreiss and Lorenz 1989), which states that if the solution of a symmetric hyperbolic system is to vary smoothly, then a number of time derivatives must be of the order unity. In particular, this should be satisfied at the initial time. BDI-derived dynamical constraints based on dynamic governing equations scaled in terms of the advective timescale. Thus the smoothness of the BDI solution is defined relative to the advective timescale. BDI derives initial data so that a number of time derivatives of the dependent variables at the initial time are of order unity. As a result, a number of dynamical constraint equations are derived to meet this criterion for smooth solutions. Based on partial differential equations (PDEs) governing numerical models, the time derivatives in the constraint equations can be expressed in terms of spatial derivatives and result in elliptic equations. Thus, BDI converts the initial value problem for hyperbolic equations to the static boundary value problem for elliptic equations. The bounded derivative principle provides an effective and general way to reduce the amplitude of fast waves in initial data. Unlike the nonlinear normal mode initialization (NMI) that eliminates fast waves by projecting the slow mode to the slow manifold in spectral space (Machenhauer 1977), the bounded derivative principle undertakes this task directly in physical space. Both BDI and NMI are static initialization schemes. Other alternative initialization methods involving time integration of a numerical model became available in recent years. For example, Lynch and Huang (1992) proposed a digital filtering approach that integrates the forecast model forward and backward in time to damp high-frequency oscillations in the adiabatic atmosphere. Huang and Lynch (1993) further extended their study to include the moisture fields.

BDI was first applied to shallow water equations in a channel by Browning et al. (1980), and then to shallow water equations with open boundaries by Browning and Kreiss (1982). In the context of the baroclinic primitive equation model, Kasahara (1982) demonstrated in theory that BDI and nonlinear NMI are identical to the degree of approximation expected from the quasigeostrophic assumption employed in the study. This theoretical conclusion was reinforced by Semazzi and Navon (1986) in a real data simulation with a global nonlinear barotropic model that showed the two methods lead to similar balanced initial states. Bijlsma and Hafkenscheid (1986) came to a similar conclusion in their real data study, specifically that BDI and NMI produced equally satisfactory results, with BDI requiring less computation than NMI. Although NMI has proven very successful in global models, its construction of normal modes over limited areas for mesoscale models is difficult, if not impossible. On the contrary, well-posed lateral boundary conditions can be naturally included in BDI through elliptic equations without the projection of analyzed fields onto the spectral space.

To extend BDI to three-dimensional baroclinic limited-area models, Browning and Kreiss (1986) studied the nonhydrostatic, hyperbolic equations commonly used in weather forecasting. They concluded that BDI should not be applied directly to these equations because of the extreme skewing of the equations when used in predicting large-scale motions. To remedy the skewness problem, they proposed the ''approximate'' system, in which the hydrostatic terms in the vertical momentum equation are multiplied by a constant α, called the quasi-nonhydrostatic constant. This constant, when chosen between 0 and 1, is designed to slow down the vertical propagating small-scale fast waves. However, it also affects the larger-scale adjustment processes such as hydrostatic adjustment. Since the hydrostatic adjustment has been degraded, it is important to obtain balanced initial fields with the effect of α included in the initialization scheme. The BDI is developed to include the quasi-nonhydrostatic constant in the initialization formulation. The approximate system was analyzed and used in a real data large-scale simulation initialized with BDI for large-scale flows (Browning and Kreiss 1986). Browning and MacDonald (1993) further incorporated topography into the approximate system formulated on the terrain-following coordinate. MacDonald et al. (2000a) used the term ''quasi-nonhydrostatic'' to refer to models that use the approximate equations. MacDonald et al. (2000b) showed that this approach may be valuable for mesoscale weather prediction, particularly of clouds and precipitation.

The 9 March storm was caused by an upper-level trough and cutoff low that moved over the Colorado Front Range. This upper-level low pressure system approaching from the southwest coincided with the low-level intrusion of an arctic cold front from the northeast. The upper-level low and the surface front created a weather pattern of strong northeasterly upslope flow, which typically causes heavy snow along the Front Range. In this case, almost 60 cm of snow fell from Boulder to Ft. Collins in less than 24 h. Most of the heavy precipitation occurred during 0000–0600 UTC on 9 March. In addition to the heavy precipitation, the storm also created strong winds of 20 m s^{-1} with gusts up to 25 m s^{-1}. The upper-level low and surface arctic front interacted with the Rocky Mountain high terrain producing heavy orographic precipitation, an ideal case for testing BDI and QNH over complex terrain. Detailed synoptic discussions of the 9 March storm may be found in Cunning and Williams (1993) and Snook (1994).

In this study, we focus on the smooth numerical solution over complex terrain, precipitation simulation over the Colorado Front Range. Section 2 shows the derivation of BDI dynamical constraints for mesoscale models based on the smooth solution. In section 3, we derive elliptic equations from these constraints based on the QNH dynamical equations. These elliptic equations

are formulated on the terrain-following coordinate to account for complex terrain. We also discuss the choice of well-posed boundary conditions for these elliptic equations when they are solved numerically. Section 4 shows the numerical results, and conclusions are given in section 5.

2. BDI dynamical constraints

BDI derives dynamical constraints on the initial data equal in number to those of the fast modes to be suppressed in the model. For smooth solutions these dynamical constraints are derived based on the dynamic governing equations in Cartesian coordinates shown in the following:

$$u_t + uu_x + vu_y + wu_z + \frac{1}{\rho_0}p'_x - fv = 0, \quad (1)$$

$$v_t + uv_x + vv_y + wv_z + \frac{1}{\rho_0}p'_y + fu = 0, \quad (2)$$

$$w_t + uw_x + vw_y + ww_z + \frac{1}{\rho_0}p'_z + \frac{\rho'}{\rho_0}g = 0, \quad (3)$$

$$\rho'_t + u\rho'_x + v\rho'_y + w\rho'_z$$
$$+ [\rho_0(u_x + v_y) + (w(\rho_0)_z + \rho_0 w_z)] = 0, \quad (4)$$

$$p'_t + up'_x + vp'_y + wp'_z + \gamma p_0(u_x + v_y + w_z)$$
$$- \rho_0 gw = 0, \quad (5)$$

where t is for time and x, y, z are the independent variables denoting, respectively, the east, north, and the vertical direction. Their corresponding velocity components in Cartesian coordinates are denoted as $u, v,$ and $w,$ respectively. The horizontal means of the density and pressure are denoted as ρ_0 and p_0, with ρ', p' as perturbation quantities from ρ_0 and p_0. The Coriolis parameter is $f,$ and g is the gravitational constant. The constant γ is defined as the ratio of c_p/c_v with c_p, c_v denoted as the specific heat at constant pressure and at constant volume, respectively. The above governing equations are the momentum equations (1), (2), and (3), the continuity equation in density (4), and the pressure equation (5). The pressure equation is used in QNH as the continuity equation and is also listed to aid the derivation of the elliptic equations in the next section.

Scale analysis is a suitable method for evaluating the magnitudes of various terms in the governing equations. The relative magnitudes of the terms may be determined by the representative magnitudes of the independent and dependent variables in different scales of motion. For the large-scale and mesoscale motions, the following typical velocity, length and depth scales are used to determine the magnitudes of various terms. The length scales, $L,$ are 10^6 m for the large-scale and 10^5 m for the mesoscale. The horizontal velocity magnitude, $\mathbf{V},$ is 10 m s^{-1}, and the vertical velocity magnitude, $W,$ are

10^{-2} m s^{-1} for the large-scale and 1 m s^{-1} for the mesoscale. The atmosphere scale height and the vertical scale of motion are chosen as $D = 10^4$ m. Based on these scaling parameters, the dimensionless governing equations are written as follows in terms of $\varepsilon = 10^{-1}$:

$$u_t = -uu_x - vu_y - \varepsilon^n wu_z - \varepsilon^{-n}\left(\frac{1}{\rho_0}p'_x - fv\right), \quad (6)$$

$$v_t = -uv_x - vv_y - \varepsilon^n wv_z - \varepsilon^{-n}\left(\frac{1}{\rho_0}p'_y + fu\right), \quad (7)$$

$$w_t = -uw_x - vw_y - \varepsilon^n ww_z - \varepsilon^{-4n-2}\left(\frac{1}{\rho_0}p'_z + \frac{\rho'}{\rho_0}\right), \quad (8)$$

$$p'_t = -up'_x - vp'_y - \varepsilon^n wp'_z$$
$$- \varepsilon^{-3+n}[\gamma p_0(u_x + v_y + \varepsilon^n w_z) - \varepsilon^n w\rho_0], \quad (9)$$

$$\rho'_t = -u\rho'_x - v\rho'_y - \varepsilon^n w\rho'_z$$
$$- \varepsilon^{-3+n}[\rho_0(u_x + v_y) + \varepsilon^n(w(\rho_0) + \rho_0 w_z)], \quad (10)$$

where

$$n = \begin{cases} 1 & \text{for } L \sim 10^6 \text{ m} \\ 0 & \text{for } L \sim 10^5 \text{ m}. \end{cases}$$

Note that all variables in Eqs. (6)–(10) are dimensionless. These dimensionless governing equations are the same as those shown in Browning and Kreiss (1986, 1997) for large-scale and mesoscale motions. Definitions of the dynamic variables in Eqs. (6)–(10) as constraint variables of a, b, c, d are shown in the following:

$$a = \frac{1}{\rho_0}p'_x - fv, \quad (11)$$

$$b = \frac{1}{\rho_0}p'_y + fu, \quad (12)$$

$$c = \frac{1}{\rho_0}p'_z + \frac{\rho'}{\rho_0}, \quad (13)$$

$$d = \gamma p_0(u_x + v_y + \varepsilon^n w_z) - \varepsilon^n w\rho_0. \quad (14)$$

Thus, we can write the dimensionless equations

$$u_t = -uu_x - vu_y - \varepsilon^n wu_z - \varepsilon^{-n}a, \quad (15)$$

$$v_t = -uv_x - vv_y - \varepsilon^n wv_z - \varepsilon^{-n}b, \quad (16)$$

$$w_t = -uw_x - vw_y - \varepsilon^n ww_z - \varepsilon^{-4n-2}c, \quad (17)$$

$$p'_t = -up'_x - vp'_y - \varepsilon^n wp'_z - \varepsilon^{-3+n}d. \quad (18)$$

We assume initial data as well as $a, b, c,$ and d are smooth, that is, they and their spatial derivatives are $O(1)$. Thus, the first-order time derivatives of dependent variables, $u_t, v_t, w_t,$ and p_t are $O(1)$ if $\varepsilon^{-n}a, \varepsilon^{-n}b, \varepsilon^{-4n-2}c,$ and $\varepsilon^{-3+n}d$ are less than or equal to $O(1)$. For example, in large-scale motions ($n = 1$), the scaling

constants associated with a and b are $O(1)$. Thus, u_t, v_t vary at $O(1)$ timescale if the magnitudes of a and b are less than $O(\varepsilon)$. In other words, the geostrophic approximations between pressure and wind fields in large-scale motions are valid to $O(\varepsilon)$. However, this balance is not required in the mesoscale motions ($n = 0$) where the scaling constants in front of a and b are $O(1)$.

In the vertical momentum and pressure equations, the scaling constants associated with c and d are ε^{-4n-2} and ε^{-3+n}, respectively. They are much larger than $O1$ for both large-scale and mesoscale motions. Thus, in order to have smooth evolution of w and p, the constraints $c \leq O(\varepsilon^{4n+2})$ and $d \leq O(\varepsilon^{3-n})$ should be satisfied. In other words, hydrostatic balance and incompressibility should be satisfied for the first-order time derivatives of w, p to be $O(1)$. However, it has been shown (Browning and Kreiss 1982; Kasahara 1982) that the first-order BDI is rather crude even for large-scale motions. Thus the second-order BDI for mesoscale motions should be sought.

The second-order BDI derives initial data constraints by requiring that the second-order time derivatives of u_{tt}, v_{tt}, w_{tt}, and p_{tt} are $O(1)$. The second-order time derivatives of dependent variables are obtained by taking the partial time derivatives of Eqs. (15)–(18) and are written as follows:

$$u_{tt} = (-uu_x - vu_y - \varepsilon^n wu_z)_t - \varepsilon^{-n}a_t,$$

$$v_{tt} = (-uv_x - vv_y - \varepsilon^n wv_z)_t - \varepsilon^{-n}b_t,$$

$$w_{tt} = (-uw_x - vw_y - \varepsilon^n ww_z)_t - \varepsilon^{-4n-2}c_t,$$

$$p'_{tt} = (-up'_x - vp'_y - \varepsilon^n wp'_z)_t - \varepsilon^{-3+n}d_t.$$

Since we assume a, b, c, d, and initial data are smooth functions of x, y, and z, the first-order time derivatives of u_t, v_t, w_t, p_t, and their spatial derivatives are $O(1)$. Thus, the second-order time derivatives of u_{tt}, v_{tt}, w_{tt}, and p'_{tt} are $O(1)$ if $\varepsilon^{-n}a_t$, $\varepsilon^{-n}b_t$, $\varepsilon^{-4n-2}c_t$, and $\varepsilon^{-3+n}d_t$ are less than or equal to $O(1)$. In the horizontal momentum equations, the order of magnitude for u_{tt} and v_{tt} depends on a_t and b_t, which are expressed as follows according to Eqs. (11) and (12):

$$a_t = \frac{1}{\rho_0}p'_{xt} - fv_t, \qquad b_t = \frac{1}{\rho_0}p'_{yt} + fu_t.$$

As mentioned previously, u_t and v_t and the spatial derivatives of p'_t are $O(1)$. Thus, a_t and b_t are $O(1)$ if the initial data are smooth.

In the vertical momentum equation, there is a large scaling constant, ε^{-2-4n}, in front of c_t. Thus, the constraint $c_t \leq O(\varepsilon^{2+4n})$ should be satisfied in order to have w_{tt} evolve on $O(1)$ timescale. Similarly, the scaling constant, ε^{-3+n}, in front of d_t is large for both the mesoscale and large-scale motions. Thus, p'_{tt} is $O(1)$ if $d_t \leq O(\varepsilon^{3-n})$ is satisfied. The most convenient way to choose the two constraints for the second-order BDI is to let $c_t = 0$ and $d_t = 0$. From Eqs. (13) and (14), $c_t = 0$ and $d_t = 0$ lead to the following two constraint equations:

$$p'_{zt} + \rho'_t = 0, \qquad \gamma p_0(u_{xt} + v_{yt} + \varepsilon^n w_{zt}) - \varepsilon^n \rho_0 w_t = 0.$$

These two-dimensionless constraint equations are written in dimensional form as follows:

$$p'_{zt} + \rho'_t g = 0, \qquad (19)$$

$$\gamma p_0(u_{xt} + v_{yt} + w_{zt}) - \rho_0 g w_t = 0. \qquad (20)$$

Therefore, two constraints on initial data are derived in order to have $O(1)$ evolution of w_{tt} and p'_{tt}, which are associated with fast waves in the atmosphere. In other words, two dynamic constraints are derived to suppress the fast acoustic waves that correspond to the two largest eigenvalues in the system (MacDonald et al. 2000a). These dynamic constraints are derived based on the scaled equations. Thus, the proper choice of scaling parameters is important because wrong parameters may result in unbalanced constraints. The scaling parameters adopted for this study have been successfully used in many previous studies (e.g., Browning and Kreiss 1997).

3. Formulations of elliptic equations

The dynamic constraint equations derived in BDI for smooth solutions lead to elliptic equations when their time derivative terms are replaced by spatial derivative terms based on the governing equations in the system. In this study, we derive elliptic equations for QNH based on its dynamic governing equations (see MacDonald et al. 2000b). The QNH governing equations for u, v, p are, respectively, the same as those in Eqs. (1), (2), and (5) except for the use of the terrain following coordinate. For convenience, we derive the elliptic equations on the Cartesian coordinate first, and then convert them to the terrain-following coordinate used in QNH. The QNH vertical momentum equation on the Cartesian coordinate is written as follows:

$$w_t + uw_x + vw_y + ww_z = \alpha\left[\frac{1}{\rho_0}p'_z + \left(\frac{g}{\gamma P_0}\right)p' - g\theta'\right]$$

$$= 0, \qquad (21)$$

where θ', the potential temperature perturbation, is defined as $\theta' = \theta/\theta_0 - 1$ with θ and θ_0 denoted, respectively, as the total and mean potential temperature. This equation is unique in the use of the quasi-nonhydrostatic constant, α, in front of the hydrostatic terms. Because the length scales of atmospheric motions in the horizontal are generally much larger than those in the vertical, the finite-difference forms of atmospheric models are badly skewed and are sensitive to small perturbations (Browning and Kreiss 1986). The quasi-nonhydrostatic constant is designed to remedy this problem. Equations (1), (2), (5), and (21) are QNH dynamic equations used to derive elliptic equations from the BDI constraint equations shown in (19) and (20).

To derive the elliptic equation for w, we express the

time derivative terms of p'_t and ρ'_t in Eq. (19) in terms of spatial derivative terms based on Eqs. (4) and (5)

$$\rho'_t = -[\rho_0(u_x + v_y) + (w(\rho_0)_z + \rho_0 w_z)], \quad (22)$$

$$p'_t = -\gamma p_0(u_x + v_y + w_z) + \rho_0 g w. \quad (23)$$

Note that these two equations for p'_t and ρ'_t are valid to $O(\varepsilon^3)$ for mesoscale motions as shown in the previous scale analysis. Substituting (22) and $\partial(23)/\partial z$ into the constraint Eq. (19), we obtain the following one-dimensional elliptic equation for w

$$w_{zz} - \frac{\rho_0 g}{p_0} w_z + \delta_z + (1 - \gamma)\frac{\rho_0 g}{p_0}\delta = 0, \quad (24)$$

where δ is the horizontal divergence defined as $\delta = u_x + v_y$. This elliptic equation for the vertical velocity in the Cartesian coordinate is equivalent to the differentiated form of Richardson's w-equation in the pressure coordinate (Richardson 1922). A similar elliptic w-equation in the Cartesian coordinate was also derived by Ooyama (1990) and used by DeMaria (1995) to diagnose the vertical velocity in a hydrostatic model.

We derive the elliptic equation for pressure from the second BDI dynamic constraint in Eq. (20). To replace the time derivative terms, we substitute $\partial(1)/\partial x, \partial(2)/\partial y, \partial(21)/\partial z$, and Eq. (21) into the constraint Eq. (20). After algebra, we obtain the following second derivative equation for pressure

$$p'_{xx} + p'_{yy} + \alpha p'_{zz} - \frac{\alpha}{\rho_0}(\rho_0)_z p_z + \alpha\left(\frac{\rho_0 g}{\gamma P_0}\right)^2 (\gamma - 1)p'$$

$$= \text{RHS}, \quad (25)$$

where

$$\text{RHS} = \rho_0\Bigg\{ f\zeta - \beta u + \alpha g\left(\theta'_z - \frac{\rho_0 g}{\gamma P_0}\theta'\right)$$

$$- \Bigg[(uu_x + vu_y + wu_z)_x + (uv_x + vv_y + wv_z)_y$$

$$+ (uw_x + vw_y + ww_z)_z$$

$$- \frac{\rho_0 g}{\gamma P_0}(uw_x + vw_y + ww_z)\Bigg]\Bigg\}.$$

The variable ζ is the vorticity defined as $\zeta = v_x - u_y$, and $\beta = \partial f/\partial y$. This equation is similar to the traditional nonlinear balance equation (see, e.g., Haltiner and Williams 1980) used by many others to derive the balanced pressure mainly for large-scale motions, in which the three-dimensional elliptic equation is usually simplified to two dimensions and the advection terms are neglected. However, scale analysis shows that the advection terms are $O(1)$ terms in mesoscale motions. In this study, we use the three-dimensional elliptic equation including all of the advection terms to solve the balanced pressure for mesoscale motions.

The quasi-nonhydrostatic constant, α, appears in front of p_{zz} in the above elliptic equation (25). In practice, it is specified as the square of the aspect ratio of $(\Delta z/\Delta x)^2$, where Δz and Δx are the vertical and horizontal grid spacing, respectively (Browning and Kreiss 1986). Therefore, α is always positive and the above equation is a three-dimensional elliptic equation for p. In theory, a unique solution for p always exists with proper boundary conditions for the elliptic equation. However, since the horizontal grid spacing is generally much larger than the vertical grid spacing, the finite-difference form of the elliptic equation becomes badly skewed without the constant α. In other words, for the unmodified vertical momentum equation, $\alpha = 1$, and the coefficients for the second-order derivative in the horizontal are much less than those in the vertical. As a result, convergence of a unique solution is more difficult to obtain in finite-difference form, even though in the continuous case a unique solution exists in theory. Thus, the effect of α in a hyperbolic system, such as the QNH model is to slow down the vertically propagating fast waves, and in an elliptic system is to make the elliptic equation less skewed.

To incorporate the topography into the initialization procedure, the above elliptic equations are formulated on the terrain-following coordinate defined as follows (see MacDonald et al. 2000b):

$$x' = x, \qquad y' = y, \qquad z' = \frac{z - z_b}{z_t - z_b}z_t,$$

where x', y', z' are independent variables on the terrain-following coordinate, and z_b, z_t are the geometric heights for the topography and the depth of the model, respectively. The basic transformation relations for spatial derivatives between the Cartesian and the terrain-following coordinates are (see Kasahara 1974)

$$F_x = F_{x'} - z_{x'}z'_z F_{z'}, \qquad F_y = F_{y'} - z_{y'}z'_z F_{z'},$$

$$F_z = z'_z F_{z'},$$

where F denotes a dependent variable.

Utilizing the above basic transformation equations and after lengthy algebraic manipulation, we derive the elliptic equations on terrain-following coordinates as follows:

$$w_{z'z'} - \frac{\rho_0 g}{p_0}(z'_z)^{-1}w_{z'} + (z'_z)^{-2}\frac{\rho_0 g}{p_0}\left(\frac{1}{\gamma} - 1\right)\delta + (z'_z)^{-1}\delta_{z'}$$

$$= 0, \quad (26)$$

$$p'_{x'x'} + p'_{y'y'} + (\alpha + z_{x'}^2 + z_{y'}^2)(z'_z)^2 p'_{z'z'} - 2z_{x'}z'_z p'_{x'z'} - 2z_{y'}z'_z p'_{y'z'}$$

$$- \left[z'_z(z_{x'x'} + z_{y'y'}) + 2(z_{x'}z'_{x'} + z_{y'}z'_{y'}) + z'_z\frac{\alpha}{\rho_0}(\rho_0)_z\right]p_{z'}$$

$$+ \alpha\left(\frac{\rho_0 g}{\gamma P_0}\right)^2 (\gamma - 1)p' = \text{RHS}, \quad (27)$$

where

$$\text{RHS} = \rho_0[f[(v'_{x'} - u'_{y'}) - z'_z(z_{x'}v'_{z'} - z_{y'}u'_{z'})] - \beta u'$$

$$+ \alpha g\left(z'_z\theta'_{z'} - \frac{\rho_0 g}{\gamma P_0}\theta'\right)$$

$$- \left((u'u'_{x'} + v'u'_{y'} + w'u'_{z'})_{x'}\right.$$

$$- z'_z z_{x'}(u'u'_{x'} + v'u'_{y'} + w'u'_{z'})_{z'}$$

$$- z'_z z_{y'}(u'v'_{x'} + v'v'_{y'} + w'v'_{z'})_{z'}$$

$$+ (u'v'_{x'} + v'v'_{y'} + w'v'_{z'})_{y'}$$

$$+ z'_z(u'w_{x'} + v'w_{y'} + w'w_{z'})_{z'}$$

$$\left.\left.- \frac{\rho_0 g}{\gamma P_0}(u'w_{x'} + v'w_{y'} + w'w_{z'})\right)\right],$$

where variables without prime (') are relative to the Cartesian coordinate, and those with prime are defined on the terrain-following coordinate. Note that since the QNH prognostic variable in the vertical momentum equation is w, the elliptic equation for the vertical velocity is also formulated in terms of w. The terrain transformation does not change the ellipticity of these second-order derivative equations. However, the transformation does introduce second-order cross derivative terms, $p'_{x'z'}$, $p'_{y'z'}$ that complicate the iterative processes in the elliptic solver.

Elliptic equations in theory always yield a unique solution provided boundary conditions are properly specified. In solving Eq. (26), a one-dimensional second-order PDE, two boundary conditions are needed. Since the bottom of the model is sloping topography, the kinematic boundary condition that prevents airflow through the bottom boundary is used to specify the bottom vertical velocity as follows

$$w = u'(z_b)_{x'} + v'(z_b)_{y'}.$$

The boundary condition for the top of model is not the rigid boundary condition. Instead, we specify the mixed-type (Dirichlet and Neumann) boundary condition for vertical velocity at the top based on the continuity equation

$$w_{z'} - (z'_z)^{-1}\frac{\rho_0 g}{\gamma P_0}w = -(z'_z)^{-1}\delta.$$

This equation is formulated on the terrain-following coordinate and is derived from equation (23) by neglecting p'_t. The above two boundary conditions determine the unique solution for the elliptic equation (26) that is solved numerically using the direct method (see, e.g., Lindzen and Kuo 1969).

To solve Eq. (27), a three-dimensional second-order PDE, two boundary conditions in each of the x', y', and z' direction are needed. In the x' direction, Neumann boundary conditions are specified at the western and eastern boundaries with $p'_{x'}$ calculated from the u-mo-

mentum equation in (1). Similarly, Neumann boundary conditions are used in the y' direction with $p'_{y'}$ calculated from the v-momentum equation. In the vertical direction, mixed-type boundary conditions are specified at the bottom and top of the model using the hydrostatic equation:

$$p'_{z'} + (z'_z)^{-1}\frac{\rho_0 g}{\gamma P_0}p' - (z'_z)^{-1}\rho_0 g\theta' = 0.$$

The above boundary conditions, specified at all boundaries for the limited-area domain, determine a unique solution for balanced pressure in Eq. (27). The multigrid software package, MUDPACK (Adams 1991), is used to solve the 3D elliptic equation (27) that includes the cross derivative terms that appear as a result of the terrain transformation. MUDPACK software provides efficient solutions using multigrid iteration with the nonzero boundary cross derivative terms moved to the right-hand side. The elliptic equations, (26) and (27), derived from the BDI constraint equations, are solved with proper boundary conditions for initial fields that are smooth and will evolve smoothly in well-behaved models as will be shown in the next section.

4. Numerical results

The initial and lateral boundary data for the simulation of the 9 March storm were derived from the Mesoscale Analysis and Prediction System (MAPS; Benjamin et al. 1991). The MAPS assimilates meteorological data on a 3-h cycle using a mesoscale model formulated on an isentropic/sigma hybrid coordinate in the vertical and a polar stereographic projection in the horizontal. MAPS data assimilation system includes asynoptic data sources such as hourly wind profiler data, automated aircraft observations, and surface observations. This allows MAPS to provide detail in mesoscale analysis using a 60 km $\times$ 60 km horizontal grid mesh, and with 25 vertical levels at 3-h intervals. MAPS mesoscale analysis provides accurate initial condition for mesoscale models.

The isentropic MAPS system assimilates meteorological variables including pressure, Montgomery streamfunction, virtual temperature, condensation pressure, and horizontal wind components on a polar stereographic projection. These variables were converted to Kelvin temperature, geopotential height, relative humidity, and the horizontal wind components on isobaric levels using a subroutine provided by MAPS (S. Benjamin 1996, personal communication). The horizontal wind components projected on the polar stereographic coordinate were rotated relative to the Lambert coordinate used by QNH. The dependent variables in QNH, such as specific humidity and virtual potential temperature, were also derived from MAPS temperature and relative humidity fields. Finally, interpolation schemes were used to convert dependent variables such as pressure, virtual potential temperature, specific humidity,
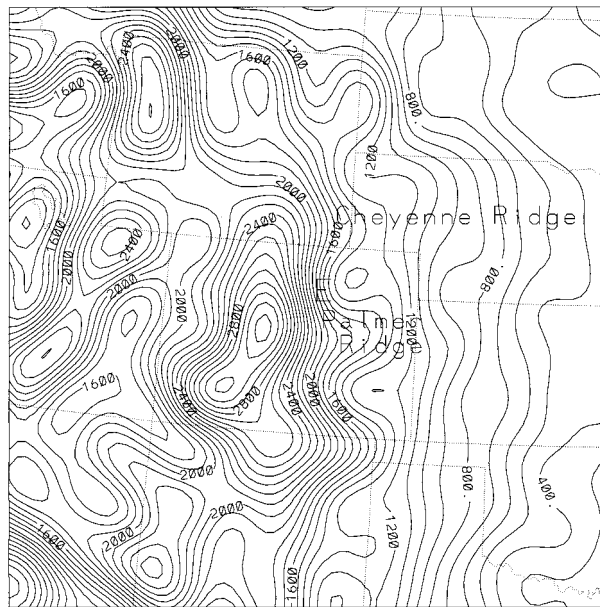
FIG. 1. Model horizontal domain and smooth topography over the Rocky Mountains used in this study. The locations of Palmer Ridge, Cheyenne Ridge, and point E are shown as labeled.

and the horizontal wind components to the QNH model grid with the Lambert projection and the terrain-following coordinate. To be consistent with the QNH model, the vertical mean pressure profile, defined as the standard atmosphere, was also removed from the total pressure field.

One of the QNH-dependent variables, vertical velocity, is not directly available and must be derived from the MAPS analysis kinematic and mass variables. In addition, due to the imbalance that may exist between the interpolated wind and mass fields, spurious large-amplitude gravity waves may be generated as well as acoustic waves, if a proper initialization is not undertaken. Thus the main purpose of BDI is to derive balanced vertical velocity and pressure for QNH as initial and lateral boundary data. The QNH model domain with smooth topography is shown in Fig. 1 over an area centered on Colorado. The smooth topography was obtained with the Fourier decomposition applied to the 5-km raw topographical data over North America and truncated shortwaves for wavelengths smaller than 200 km. Figure 1 shows that the peak of the smoothed Rocky Mountain is about 3200 m. Point E in Fig. 1 was chosen for the evolution of the numerical solution to be shown later. The model domain in the horizontal covers about 1500 km $\times$ 1500 km, with a horizontal resolution of 20 km used in this study. Its vertical range includes the whole troposphere and the lower stratosphere with a model top height of 16 km and a vertical resolution of 500 m. The quasi-nonhydrostatic parameter in this study is $\alpha = (0.5/20)^2 \approx 10^{-3}$.

To simulate the 9 March storm, we derived smooth initial fields from the MAPS analysis data at 1200 UTC

on 8 March 1992 using the elliptic solvers. We solved the one-dimensional elliptic equation (26) for smooth initial vertical velocity using the MAPS interpolated kinematic and mass fields with the proper boundary conditions described previously. The derived vertical velocity was used to recompute the horizontal divergence based on the continuity equation shown in (23). The divergence together with the vorticity was used to recompute the horizontal wind components based on the Helmholtz relationships (see Browning and Kreiss 1986; Lee and Browning 1994). As pointed out by Browning and Kreiss (1986), the recomputational process is reversible in the continuum and should be numerically reversible, although limited by truncational error. Thus, the recomputation of the horizontal wind was used as a static check on the noise in the data. The wind and temperature fields were used to solve for the smooth initial pressure based on the three-dimensional elliptic equation (27) with proper boundary conditions. The temperature and water vapor fields were kept the same as those interpolated from the MAPS analysis data. The initial cloud water and cloud ice, rain, snow, and graupel were not available and were set to zero at the start of the integration as well as at the lateral boundary during the model integration.

The above initialization procedures do not include condensational heating terms because no appreciable precipitation was observed over the model domain at the time of initialization, that is, 1200 UTC 8 March 1992. However, it is important to note that condensational heating should be included in BDI if heavy precipitation occurred at the time of initialization. The aforementioned procedures, including interpolation and elliptic solvers for initial data, were repeated for lateral boundary data using MAPS analyses at 3-h intervals through the 48-h simulation period. In a real forecast, it is impossible to have analysis data beyond the initial time for lateral boundary conditions. Thus, lateral boundary data, in practice, should be derived from forecasts. Unfortunately, MAPS provides only a 12-h forecast, which is much less than the 48-h integration undertaken in this study. The accuracy of a limited-area model forecast depends on the model error itself as well as the lateral boundary data error inherited from another model. Thus, the use of MAPS analysis for lateral boundary data allows us to separate errors in BDI and QNH from forecast errors in MAPS. The boundary data at 3-h intervals were interpolated every time step in the numerical simulation to update the QNH lateral boundary conditions, based on the characteristic equations described in Browning and Kreiss (1986) and MacDonald et al. (2000a).

The initial pressure and wind fields obtained from the elliptic solvers are displayed on the terrain-following coordinate[1] at $z' = 750$ m shown in Figs. 2a and 2b.

---

[1] Unless it is otherwise stated, all figures are displayed on the terrain-following coordinate.
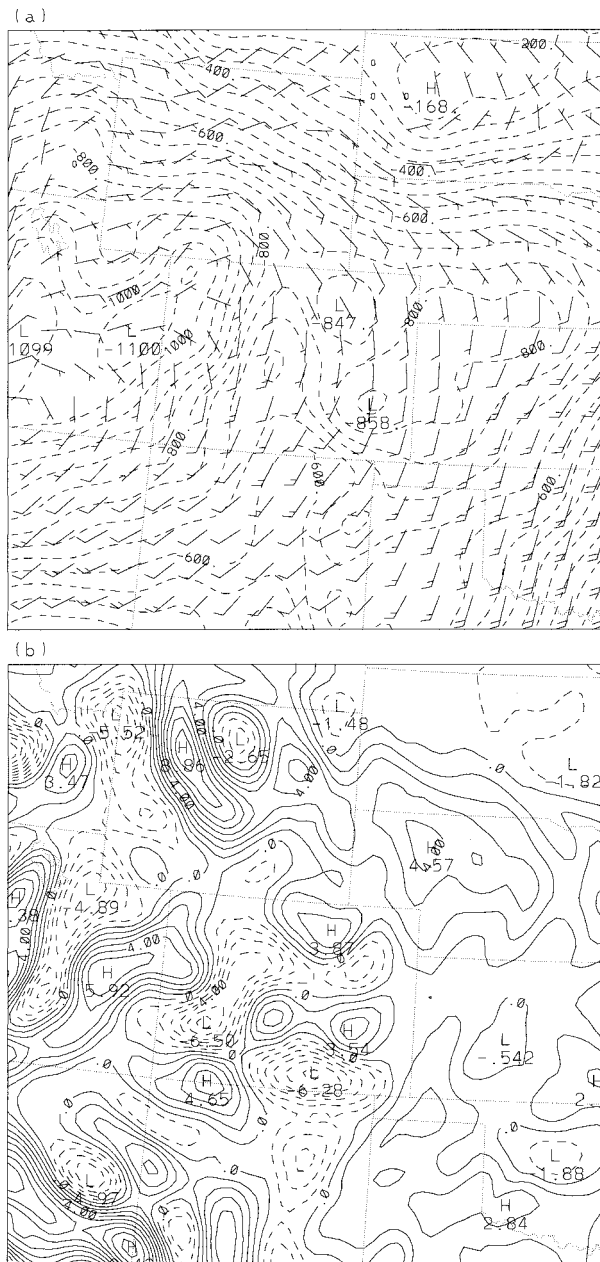
FIG. 2. The model initial data at 1200 UTC 8 Mar 1992, derived from the elliptic solvers are displayed at $z' = 750$ m for (a) the horizontal wind (full and half-barb denote 10 and 5 m s^{-1}, respectively) and pressure perturbation (contour lines every 50 Pa) fields, and (b) the vertical velocity field in cm s^{-1} with positive (negative) sign for upward (downward) motions.

Figure 2a shows the horizontal wind vector superimposed over the perturbation pressure (pascals) field, which is depicted as dashed contours. The pressure field was mainly determined by the wind and temperature fields through the three-dimensional elliptic solver. In the northern part of the domain, the horizontal wind field was basically northeasterlies, while in the south,

it was southerlies or southwesterlies. The northerlies that were adjacent to southerlies were associated with the surface front located near the border of Nebraska and South Dakota. The vertical velocity shown in Fig. 2b was closely related to the horizontal wind and topography. The upward (downward) motions were mainly associated with upslope (downslope) winds. The accuracy of BDI is examined by the fit of BDI-derived wind and pressure to radiosonde observations at 500 hPa and 300 hPa over a period of one week from 12 May to 18 May 1998. The root-mean-square differences for the wind and height fields at 500 (300) hPa are 4.6 (5.3) m s^{-1} and 15.1 (16.1) m, respectively.

With the initial and lateral boundary data derived from the elliptic solvers, QNH was numerically integrated for 48 h to demonstrate the smooth transition of the storm moving in and out of the model domain without causing lateral boundary discontinuities. Figures 3a–c show QNH simulations of horizontal wind and pressure at the height of $z' = 5250$ m on the initial hour, 6 and 12 h to demonstrate the storm smoothly entering the model domain. Figure 3a shows that at 1200 UTC 8 March the upper-level low was initially centered at the southwest of Four Corners and was located partially outside of the model domain. After 6 h at 1800 UTC, Fig. 3b shows the low continued to move into the domain and approached Four Corners. Figure 3c shows the storm 12 h into the simulation at 0000 UTC on 9 March. The low was largely inside the model domain and located east of Four Corners. During the first 12-h simulation, when the storm smoothly entered the model domain, there was no trace of lateral boundary discontinuity problems. In the next 12- to 24-h, the upper-level low continued to move eastward and then northeastward after passing across the Rocky Mountain Front Range.

Figure 4a shows the simulation after 36 h at 0000 UTC 10 March. The low weakened and became an upper-level trough. The trough approached the eastern side of the boundary and smoothly exited out of the model domain on 0600 UTC as shown in Fig. 4b. Figure 4c shows that the trough was completely outside the model domain after the 48-h simulation. During the last 12 h of the simulation, when the storm smoothly exited the model domain, we did not find any noise reflection from the eastern boundary. The root-mean-square differences for the wind and pressure between the QNH simulation and MAPS analysis at $z' = 5250$ m are computed. These differences are about the same size as those typically found between MAPS analysis and radiosonde observations. Note that there is no lateral boundary transitional zone nor top sponge layers to numerically damp noise caused by the boundary discontinuity. The domain boundaries shown in the figures are the lateral boundaries used in the model.

To examine the smooth evolution of the QNH solution, we show the temporal variation of the numerical
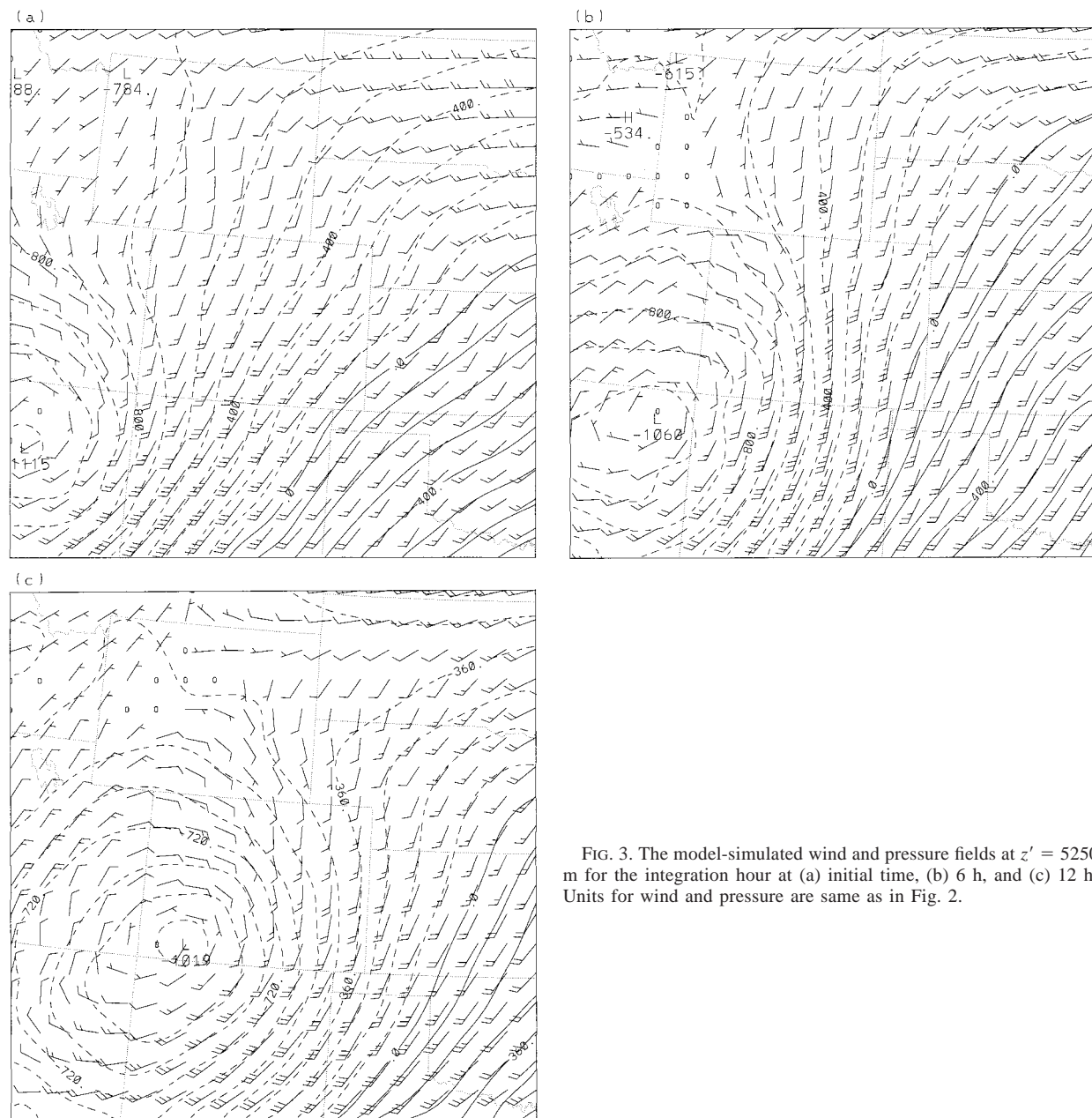
(a)

(b)

(c)

FIG. 3. The model-simulated wind and pressure fields at $z' = 5250$ m for the integration hour at (a) initial time, (b) 6 h, and (c) 12 h. Units for wind and pressure are same as in Fig. 2.

solution at different altitudes at the location[2] shown as point E in Fig. 1. Since fast waves have more direct impact on the model variables of p and w than those of u, v, and θ, we have shown[3] the evolution of p and w for 48 h in Figs. 5a, b. For the pressure graph shown in Fig. 5a, there were large-scale slow variations over

48 h, upon which high temporal variations caused by acoustic waves were superimposed. It is apparent that these high temporal variations had no significant impact on the large-scale trends, except causing them to wiggle slightly. The pressure evolution generally was less smooth at low levels over steep mountains than at middle and high levels with smooth terrain. This is because the more steep the mountain, the easier smaller-scale fast waves can be excited by impinging low-level winds (see Browning and MacDonald 1993).

The vertical velocity evolved smoothly during the 48-h period as shown in Fig. 5b. Its evolution at various

---

[2] Temporal variations at other geographical locations were examined and the results were similar.

[3] The evolution of numerical solutions for u, v and θ (not shown) were very smooth at all levels.
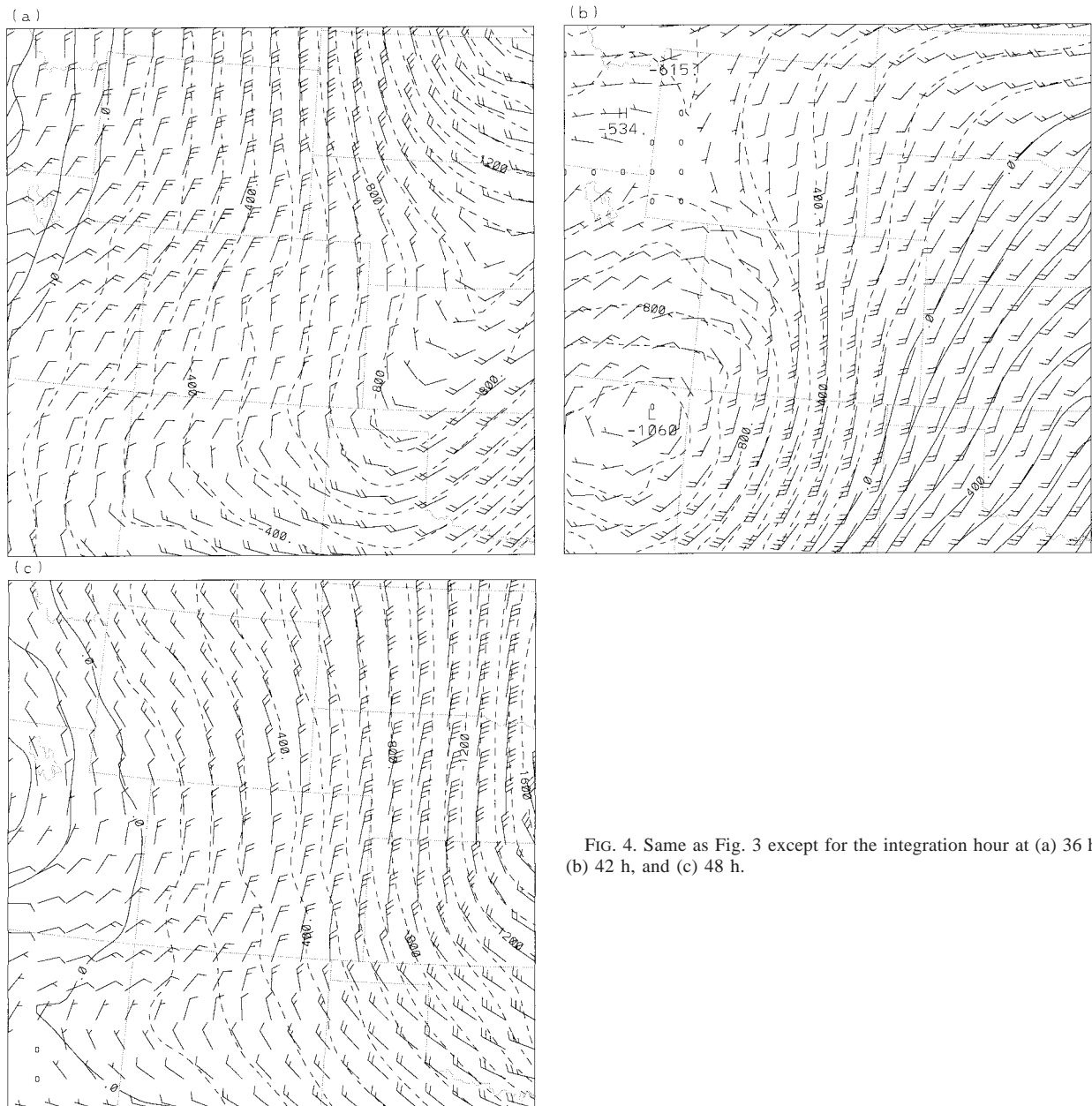
(a)

(b)

(c)

Fig. 4. Same as Fig. 3 except for the integration hour at (a) 36 h, (b) 42 h, and (c) 48 h.

heights was smoother than that of pressure because the effect of fast waves on the vertical velocity was greatly reduced by the quasi-nonhydrostatic parameter. The most significant vertical velocity changes occurred during 12- to 24-h, which coincided with the 12-h active period of the storm in the region. The arctic front moved into the region at around 0000 UTC on 9 March and caused heavy snow in the following 12 h (Snook 1994). In particular, most of the snowfall occurred from 0000 UTC to 0600 UTC, that is, the integration period from 12 to 18 h. The 6-h period of heavy snowfall coincided with the most rapid vertical velocity increases at low and middle levels, where strong condensation occurred

during 0000–0600 UTC. After 0600 UTC, the storm started to move eastward and the vertical velocity rapidly decreased. These changes in vertical velocity were consistent with the pressure tendencies shown in Fig. 5a. The pressure decreased before 0600 UTC 9 March, with the approaching of the arctic front and then increased after the front passed through. Also low-level temperature (not shown) decreased rapidly after the arctic cold front moved into the region while temperature in the middle troposphere increased due to the large amount of condensational heating.

To depict the geographic structure of the storm, figures will be presented for low-level easterlies, pressure,
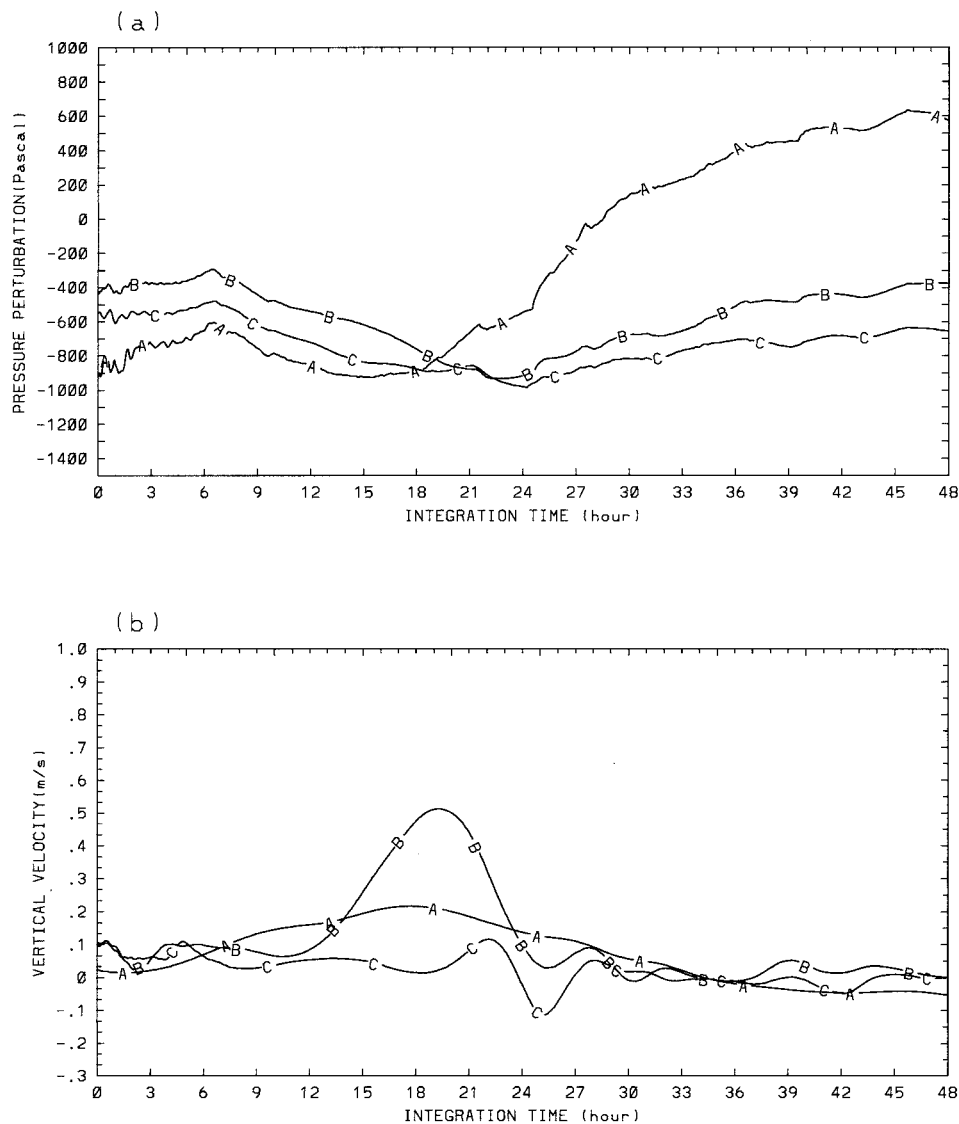
FIG. 5. The 48-h evolutions for (a) pressure perturbation, (b) vertical velocity at point E on different altitudes. Curves A, B, and C correspond to the altitude of $z' = 250$ m, 5250 m, and 9250 m, respectively.

vertical velocity, and precipitation. Figures 6a and 6b show the 12-h simulated pressure and wind fields at 0000 UTC 9 March at $z' = 750$ m. Figure 6a shows the low pressure system was located over eastern Colorado and western Kansas. To the north, the high pressure dominated with the prevalent northeasterlies. Strong upslope easterlies were found over the northeastern part of Colorado. Southeasterlies in eastern Colorado and western Kansas carried in an abundant supply of moisture from the south. The easterlies impinged upon the Rocky Mountains and resulted in the upward motions shown in Fig. 6b. The important feature of the vertical velocity over Colorado was the upward motion with the maximum of 0.21 m s^{-1} centered over northeastern Colorado. This maximum of vertical velocity extended to the south-southeast corresponding to the

low pressure system along the Colorado Front Range. The vertical velocity field was closely related to the geographical distribution of horizontal wind and topography over the Front Range. For example, with the predominant easterlies and northeasterlies over the region, the upward motions were found over Cheyenne Ridge and Palmer Ridge (see Fig. 1 for locations). In between, there was downward motion associated with the downslope wind.

Figures 7a and 7b are similar to Figs. 6a and 6b, respectively, except for 0600 UTC, at which time the northeasterlies over northeastern Colorado intensified to an average speed of 20 m s^{-1}. Comparisons of Figs. 7a and 6a show that the low pressure continued to deepen and to dominate eastern Colorado and western Kansas from 0000 to 0600 UTC. At 0600 UTC, the low pressure
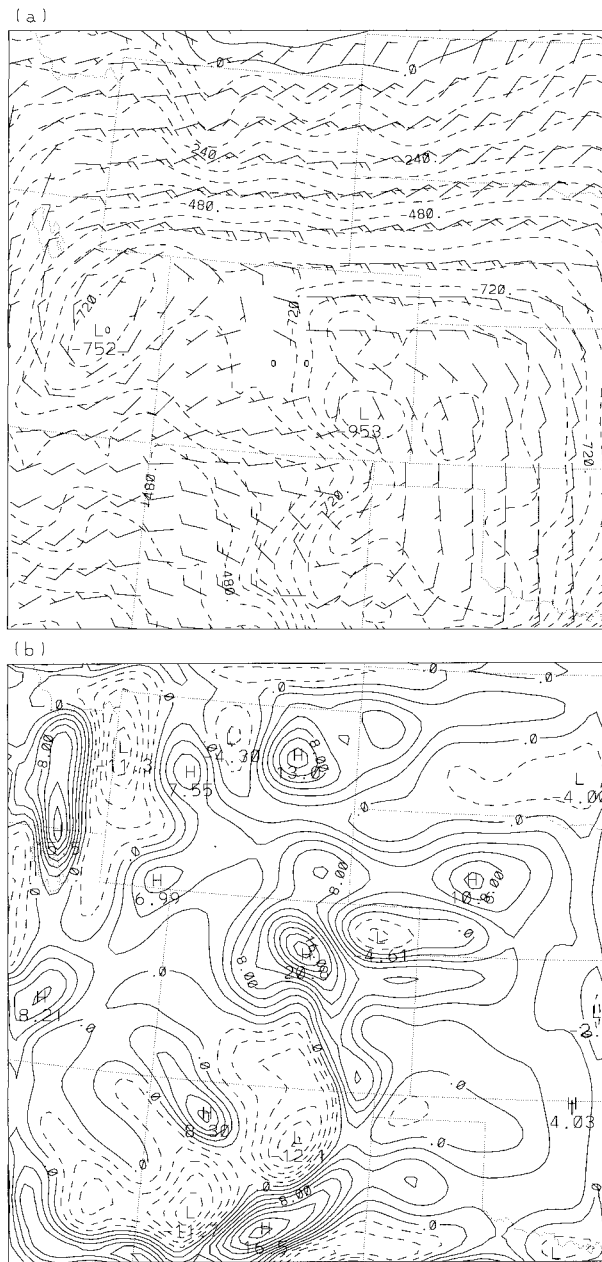
FIG. 6. The model-simulated (a) horizontal wind and pressure, (b) vertical velocity on $z' = 750$ m simulated at 12 h, i.e., 0000 UTC 9 Mar. Units for wind and pressure are the same as in Fig. 2.

FIG. 7. Same as Figs. 6a and 6b except for the 18-h simulation at 0600 UTC 9 Mar.

center had moved eastward and was located at the northwestern corner of Kansas. As the result of this change in pressure, the southeasterly (upslope) flow over the south of Palmer Ridge at 0000 UTC became southwesterly (downslope) at 0600 UTC. Consequently, the vertical velocity in this region changed accordingly, that is, from the upward motion at 0000 UTC to downward motion at 0600 UTC as shown in Fig. 7b. It is also evident that the vertical velocity at 0600 UTC was considerably larger than that at 0000 UTC. Despite the
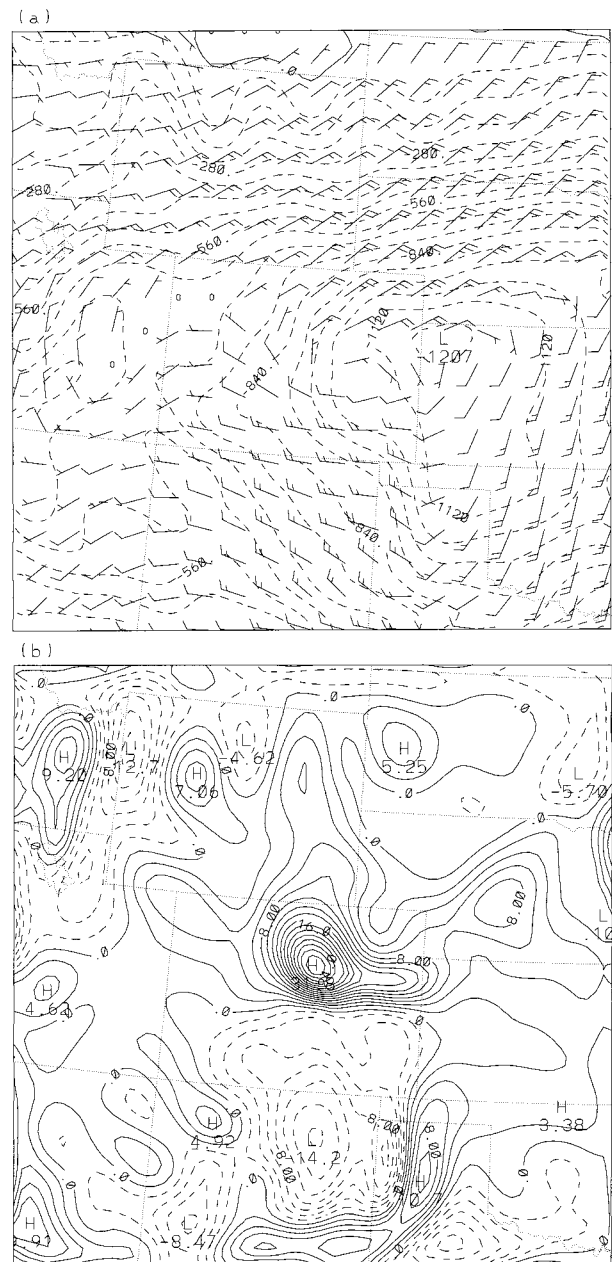
aforementioned differences, the two most prominent features that resulted in heavy precipitation were the persistent easterlies and strong upward motions located over northeast Colorado. The maximum vertical velocity in both Figs. 6b and 7b was located along the Front Range where the heaviest snow fell along the steep slope of the Rocky Mountains.

Figures 8 and 9 showed, respectively, the model-simulated and the observed 24-h precipitation accumulated from 1200 UTC on 8–9 March 1200 UTC. The model-simulated and observed precipitation patterns were in
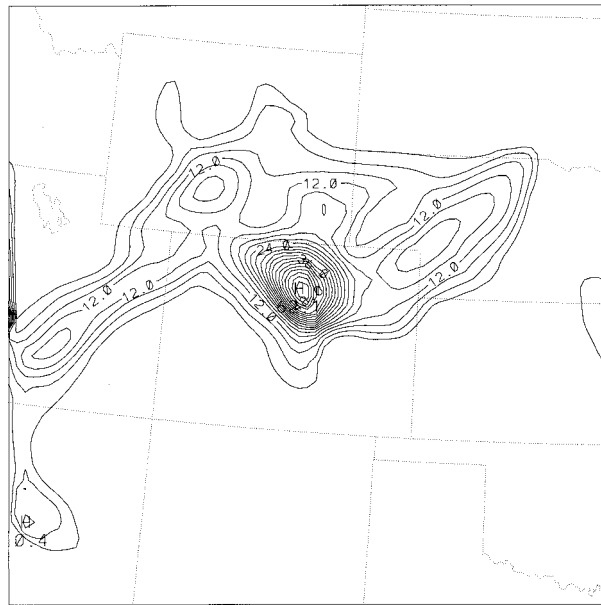
FIG. 8. The model-simulated 24-h accumulated precipitation (mm) from 1200 UTC 8 Mar to 1200 UTC 9 Mar.

the ''snow-drifting'' problem caused by the strong low-level winds of 20 m s^{-1} associated with the storm. The maximum precipitation amount simulated by the model, about 60 mm melted water (equivalent to 2 ft of snow), was closer to the snow that actually fell in Boulder than that of observed data shown in Fig. 9. Despite the discrepancy in precipitation amounts, the threat score computed based on the threshold of 20 mm in Figs. 8 and 9 was about 0.5. It is noted that relative dense precipitation contours in Fig. 8 near the western boundary in Utah are caused by the lack of cloud fields such as cloud water and cloud ice at lateral boundaries.

In this case, we have found the simulated precipitation was not sensitive to the choice of α. Based on the model grid intervals, α was specified as $(0.5/20)^2$, which is less than 10^{-3}. We have repeated the numerical simulations with α chosen as $4 \times (0.5/20)^2$ and $16 \times (0.5/20)^2 = 10^{-2}$. The results were similar despite the use of a different α. This is consistent with a study by Browning and Kreiss (1997). They showed both analytically and numerically in a heating case, that the numerical solution was dominated more by the heating than by the choice of α.

5. Summary and conclusions

This study presents the first application of mesoscale BDI and the first real data simulation for the QNH model. We have successfully demonstrated that BDI and QNH are able to produce a smooth numerical solution

good agreements with both of the maximum precipitation zones along the steep slope of the Rocky Mountain Front Range. However, the simulated precipitation amounts were substantially higher than the observed amounts. It is possible that the observed precipitation amounts shown in Fig. 9 were underestimated due to
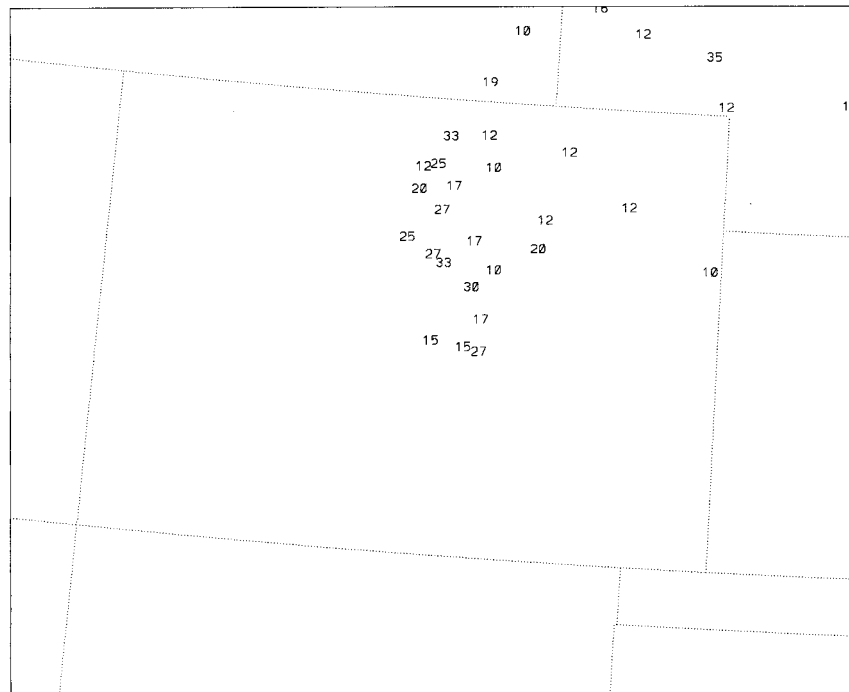

FIG. 9. The observed precipitation (mm) over Colorado accumulated 24 h from 1200 UTC 8 Mar to 1200 UTC 9 Mar.

and good precipitation simulation over the high terrain associated with the Rocky Mountains. Following a scale analysis for mesoscale motions, we derived the second-order BDI from which two dynamic constraint equations are obtained. These constraints suppress fast acoustic waves associated with the two largest eigenvalues in the system (see MacDonald et al. 2000a). The first dynamic constraint leads to a one-dimensional elliptic equation for the vertical velocity. It is basically the same as the differentiated form of the Richardson's w equation. The second constraint yields a three-dimensional elliptic pressure equation that is similar to the so-called non-linear balance equation. These elliptic equations are used to derive smooth initial mesoscale flows over complex terrain on a limited-area domain for the QNH model.

BDI converts the initial value problem for hyperbolic equations to a static boundary value problem for elliptic equations. As a result, the lateral boundary conditions for the hyperbolic system can be naturally included through the formulation of well-posed boundary conditions for the elliptic equations. This amenability to limited domains is one of the main advantages in choosing BDI over NMI, even though both of them have been successfully applied to large-scale global models. The BDI procedures used in this study are adiabatic. Their uses are justified because no appreciable precipitation occurred over the model domain at the time of initialization. However, for daily mesoscale forecasts, it is very important to properly initialize the QNH model with diabatic heating included in the BDI procedures. The proper initialization of diabatic heating with moisture field is the key to successful weather forecasts. A number of studies have shown promising results on the use of diabatic initialization to improve the tropical analysis for tropical cyclone models or general circulation models (see, e.g., Kasahara et al. 1994; Kasahara et al. 1996; Krishnamurti et al. 1994).

The QNH model initialized with BDI faithfully simulates the 9 March storm that produced nearly 2 ft of snow in less than 24 h along the Colorado Front Range. It was one of our main goals to examine the smoothness of the QNH model solution in the presence of a mesoscale storm over complex terrain in order to test the mathematical foundation of the smooth solution (Browning and Kreiss 1986) upon which BDI and QNH are based. The numerical results show that the initial fields derived from BDI were smooth and evolved smoothly for 48 h. For the pressure evolution over 48 h, there were smooth meso- and large-scale variations, upon which small-amplitude fast acoustic waves were superimposed. The vertical velocity evolution was smooth because the quasi-nonhydrostatic parameter greatly reduced the effect of the fast waves on the vertical velocity. In addition to the smooth evolution in time, we also examined the smooth transition of the mesoscale storm near the lateral boundaries. The simulated storm smoothly entered the model domain from the western boundary, moved across the model domain, and finally exited smoothly at the eastern boundary. During the 48-h simulation, the mesoscale storm moved freely in and out of the limited-area model domain as if there were no lateral boundaries. The smooth evolution of the numerically simulated mesoscale storm reinforces the theoretical mathematical analysis on the existence of the smooth solution (Kreiss and Lorenz 1989). Based on the theory, a smooth initial solution derived using BDI evolves smoothly in a nearly symmetric hyperbolic system (such as QNH) for a period of time. In particular, the smooth solution exists up to lateral boundaries.

The 9 March storm was caused by the intrinsic interactions among the topography, upslope easterlies, vertical velocity, and precipitation, in the vicinity of high mountains. To investigate these interactions, we examined the 9 March storm extensively from various angles. They include the temporal variation at various heights where the heaviest precipitation occurred and the geographical extent of the storm. The temporal variations of the vertical velocity showed the most rapid increases during 0000–0600 UTC 9 March, at which time the heaviest precipitation fell over the region. Examination of the topography within the region affected by the storm showed that the persistent northeasterlies and strong dynamic forcing from the midtropospheric system resulted in the heavy precipitation concentrated along the Colorado Front Range. These results indicate a close relationship between the vertical velocity and precipitation. The model simulated 24-h accumulated precipitation was in good agreement with that observed during the same period.

The 9 March storm was simulated rather than forecast because lateral boundary conditions used in this study were derived from MAPS analysis data. This is done mainly because MAPS provides only a 12-h forecast, which is too short to be used as lateral boundary data in our 48-h simulation. Although the Eta model provides a 48-h prediction, its initial data may not include mesoscale features as accurate as MAPS analysis. Also, it is equally important to point out that Eta provides lateral boundary data every 6 h, which may not be frequent enough to capture the fast moving 9 March storm. Furthermore, the use of MAPS analysis data for lateral boundary conditions allows us to focus on the accuracies of BDI and QNH without the contamination of forecast errors from other models. Although the results shown in this study are by no means a forecast, we believe it does not seriously diminish the objectives of this study. We are currently utilizing BDI and QNH for real-time mesoscale weather forecasting using lateral boundary data derived from Eta model forecasts.

his help in obtaining MAPS data and codes for processing the data. We thank Dr. John Adams for providing us with the multigrid software package for the elliptic solvers. Thanks are also given to Dr. Joann Dennett for the editorial review and to Paul Schultz, Edward Tollerud, and Barry Schwartz for their help in obtaining topographical and precipitation data. Finally, we greatly appreciate the valuable comments and criticism made by Dr. Ying-Hwa Kuo and the anonymous reviewers during the review process.

REFERENCES

Adams, J., 1991: Recent enhancements in MUDPACK: A multigrid software package for elliptic partial differential equations. *Appl. Math. Comput.,* **43,** 79–94.

Bengtsson, L., 1975: Four-dimensional data assimilation of meteorological observations. World Meteorological Organization GARP Publ. No. 15, 76 pp.

Benjamin, S. G., K. A. Brewster, R. Brummer, B. F. Jewett, T. W. Schlatter, T. L. Smith, and P. A. Stamus, 1991: An isentropic three-hourly data assimilation system using ACARS aircraft observations. *Mon. Wea. Rev.,* **119,** 888–906.

Bijlsma, S. J., and L. M. Hafkenscheid, 1986: Initialization of a limited area model: A comparison between the nonlinear normal mode and bounded derivative methods. *Mon. Wea. Rev.,* **114,** 1445–1455.

Browning, G. L., and H.-O. Kreiss, 1982: Initialization of the shallow water equations with open boundaries by the bounded derivative method. *Tellus,* **34,** 334–351.

——, and ——, 1986: Scaling and computation of smooth atmospheric motions. *Tellus,* **38,** 295–313.

——, and A. E. MacDonald, 1993: Incorporating topography into the multiscale systems for the atmosphere and oceans. *Dyn. Atmos. Oceans,* **18,** 119–149.

——, and H.-O. Kreiss, 1997: The role of gravity waves in slowly varying in time mesoscale motions. *J. Atmos. Sci.,* **54,** 1166–1184.

——, A. Kasahara, and H.-O. Kreiss, 1980: Initialization of the primitive equations by the bounded derivative method. *J. Atmos. Sci.,* **37,** 1424–1436.

Cunning, J. B., and S. F. Williams, 1993: *STORM-FEST Operations Summary and Data Inventory.* NOAA/U.S. Weather Research Program Office, 389 pp.

Daley, R., 1991: *Atmospheric Data Analysis.* Cambridge University Press, 457 pp.

DeMaria, M., 1995: Evaluation of a hydrostatic, height-coordinate formulation of the primitive equations for atmospheric modeling. *Mon. Wea. Rev.,* **123,** 3576–3589.

Haltiner, G., and R. Williams, 1980: *Numerical Prediction and Dynamic Meteorology.* Wiley and Sons, 477 pp.

Huang, X.-Y., and P. Lynch, 1993: Diabatic digital-filtering initialization: Application to the HIRLAM model. *Mon. Wea. Rev.,* **121,** 589–603.

Kasahara, A., 1974: Various vertical coordinate systems used for numerical weather prediction. *Mon. Wea. Rev.,* **102,** 509–522.

——, 1982: Nonlinear normal mode initialization and the bounded derivative method. *Rev. Geophys. Space Phys.,* **20,** 385–397.

——, A. P. Mizzi, and L. J. Donner, 1994: Diabatic initialization for improvement in the tropical analysis of divergence and moisture using satellite radiometric imagery data. *Tellus,* **46A,** 242–264.

——, J. I. Tsutsui, and H. Hirakuchi, 1996: Inversion methods of three cumulus parameterizations for diabatic initialization of a tropical cyclone model. *Mon. Wea. Rev.,* **124,** 2304–2321.

Kreiss, H.-O., 1980: Problems with different time scales for partial differential equations. *Comm. Pure Appl. Math.,* **18,** 399–439.

——, and J. Lorenz, 1989: *Initial Boundary Value Problems and the Navier–Stokes Equations.* Academic Press, 402 pp.

Krishnamurti, T. N., G. D. Rohaly, and H. S. Bedi, 1994: On the improvement of precipitation forecast skill from physical initialization. *Tellus,* **46A,** 598–614.

Lee, J. L., and G. L. Browning, 1994: Analysis of errors in the horizontal divergence derived from high temporal resolution of the wind. *Mon. Wea. Rev.,* **122,** 851–863.

Lindzen, R. S., and H. L. Kuo, 1969: Reliable method for numerical integration of a large class of ordinary and partial differential equations. *Mon. Wea. Rev.,* **97,** 732–734.

Lynch, P., and X.-Y. Huang, 1992: Initialization of the HIRLAM model using a digital filter. *Mon. Wea. Rev.,* **120,** 1019–1034.

MacDonald, A. E., J. L. Lee, and Y. Xie, 2000a: On the use of quasi-nonhydrostatic models for mesoscale weather prediction. *J. Atmos. Sci.,* in press.

——, ——, and S. Sun, 2000b; QNH: Design and test of a quasi-nonhydrostatic model for mesoscale weather prediction. *Mon. Wea. Rev.,* **128,** 1016–1036.

Machenhauer, B., 1977: On the dynamics of gravity oscillations in a shallow water model, with applications to normal mode initialization. *Contrib. Atmos. Phys.,* **50,** 253–271.

Ooyama, K., 1990: A thermodynamic foundation for modeling the moist atmosphere. *J. Atmos. Sci.,* **47,** 2580–2593.

Richardson, L. F., 1992: *Weather Prediction by Numerical Process.* Cambridge University Press, 236 pp.

Semazzi, F. H. M., and I. M. Navon, 1986: A comparison of the bounded derivative and the normal-mode initialization methods using real data. *Mon. Wea. Rev.,* **114,** 2106–2121.

Snook, J., 1994: An investigation of Colorado front range winter storms using a nonhydrostatic mesoscale numerical model designed for operational use. NOAA Tech. Memo. ERL FSL-10, 373 pp. [Available from Forecast Systems Laboratory, Boulder, CO 80303.]